

Spectral Inference from a Multiplexing Fourier Transform Spectrometer

Arsen R. Hajian¹, Kevin H. Knuth², Brian Pohl³, J. Thomas Armstrong⁴, David Mozurkewich⁴, Robert B. Hindsley⁴, Christopher Tycner⁵ and Robert Olling¹.

*hajian.arsen@usno.navy.mil, kevin.h.knuth@nasa.gov bpohl@physics.unc.edu,
hindsley@nrl.navy.mil, tom.armstrong@nrl.navy.mil, mozurk@nrl.navy.mil,
tycner@astro.utoronto.ca, olling@usno.navy.mil*

Received _____; accepted _____

¹Department of Astrometry, US Naval Observatory, 3450 Massachusetts Av, NW, Washington, DC 20392-5420.

²Computational Sciences Division, Code IC, NASA Ames Research Center, M/S 269-3, Moffett Field, CA 94035-1000).

³Department of Astrometry, US Naval Observatory, 3450 Massachusetts Av, NW, Washington, DC 20392-5420 (Currently at: Department of Physics and Astronomy, University of North Carolina at Chapel Hill, Phillips Hall, CB #3255, Chapel Hill, NC 27599-3255).

⁴Remote Sensing Division, Naval Research Laboratory, Code 7215, Washington, DC, 20375.

⁵Department of Astronomy and Astrophysics, University of Toronto, 60 St. George Street, Toronto, ON M5S 3H8, Canada.

ABSTRACT

We have developed a new Fourier Transform Spectrometer that disperses the white light fringe and multiplexes the output on a CCD detector. The data resulting from this instrument consist of a series of narrowband interferograms from which can be inferred a series of narrowband electromagnetic spectra. Juxtaposing the narrowband segments of the spectrum allows reconstruction of a significant fraction of the optical bandpass. In this paper, we describe a method by which the “best” narrowband spectrum can be inferred from an interferogram. The algorithm is robust, insensitive to the initial assumptions regarding the spectral energy distribution, and facilitates the implementation of a high throughput, broadband Fourier Transform spectrometer. We present two different adaptations of the algorithm: one which solves for the spectral intensity, and the other which solves for the spectral intensity as well as the lag corresponding to the central fringe in the interferogram.

1. Introduction

The past two decades have seen tremendous improvements in the capabilities of astronomical spectrometers. Velocity precisions of 1 km s^{-1} were rarely achieved prior to 1980, while the current generation of high-precision spectrometers boast precisions of a few m s^{-1} . Such instruments have been able to detect one or more companions with $0.16M_{\text{J}} < M \sin(i) < 15M_{\text{J}}$ in approximately 100 stellar systems (i is the inclination angle of the orbit of the companion and M_{J} is the mass of Jupiter). Recent progress using interferometric spectrometers for planet detection have shown initial promise (see, for example, Erskine *et al.* 2003). Summaries of the advantages and limitations of the spectroscopic instrumentation and data reduction procedures are discussed elsewhere (*c.f.*, Butler *et al.* 1996; Cumming, Marcy, & Butler 1999, Marcy & Butler 1998; Baranne *et al.* 1996, and references therein). If values of $M \sin(i)$ significantly smaller than M_{J} are to be inferred spectroscopically, it will likely require a very different type of instrument, as most of the factors limiting the performance of the currently available spectrometers are inherent to the apparatus.

To this end, we have developed a multiplexed Fourier Transform Spectrometer (FTS) equipped with a laser metrology system to precisely determine the optical path difference, and hence the wavelength scale and bandpass shape. The instrument disperses recombined white light onto a CCD array with a diffraction grating, dividing the optical band into a set of adjacent narrow spectral channels. As the lag, or delay difference, x between the interfering beams changes, each spectral channel shows intensity variations which are recorded as an interferogram, $I(x)$, from which the spectrum, $\tilde{I}(s)$, can be determined (here, s is wavenumber). One advantage of multiplexing the spectrum in this way is that it produces a gain in sensitivity (as compared to a conventional single-pixel FTS with the same total bandwidth) that is proportional to the resolving power of the grating, R_{g} . The “grating” in a conventional FTS can be considered to have $R_{\text{g}} = 1$.

A second advantage of multiplexing the FTS derives from the Nyquist rate. Interferograms from narrowband signals can be sampled at more widely spaced delay intervals than can the interferogram from a broadband signal. The reduced demands on the sampling rate allow us to increase the instrumental duty cycle and dramatically simplify the technical problems of constructing and operating the interferometer.

This paper describes a simple method for inferring the spectrum across a narrowband spectral channel given a narrowband interferogram sampled sparsely at the decreased rate. The instrumental configuration will be described in detail in a future publication, but the basic design is summarized in the next section.

In Section 3, we describe two algorithms used to infer a narrowband spectrum from an interferogram, and show that the spectrum can be accurately reconstructed from a sparsely sampled interferogram. In Section 4, we discuss the practical implications resulting from these algorithms, and conclude with a summary in Section 5.

2. The Multipixel FTS

A schematic representation of a multipixel FTS is shown in Figure 1. The light collected at the telescope is collimated and directed to the beamsplitter. The two split beams travel down delay lines, are retroreflected, and are recombined at the beam combiner. One way to improve the sensitivity of a conventional FTS is to multiplex the interferogram. As shown in Figure 1, the recombined beam is dispersed with a diffraction grating and is focused onto a CCD detector. This configuration effectively splits the white light beam into numerous narrowband beams.

Fourier Transform spectrometers have significant advantages over other spectrometer systems: they are capable of (1) providing a resolving power, $R_{\text{FTS}} = s/\delta s$, in excess of several million, [s is the wavenumber and δs is the spectral separation between adjacent, independent resolving elements] (2) accepting radiation from a very broad bandwidth and solid angle, (3) providing spectra with a configurable resolution based on the total optical delay introduced, and (4) yielding simple and well-known impulse responses. On the other hand, few astronomical FTS systems are currently being supported. The primary reason for this is poor throughput: a conventional FTS is no more sensitive than a single-pixel scanning spectrometer. A modern conventional spectrometer is usually equipped with a CCD array which multiplexes the dispersed output so that the full integration time is spent integrating on all N_{ch} spectral channels. Modern CCDs easily allow N_{ch} in excess of several thousand. By contrast, a conventional FTS with the same total bandwidth is typically N_{ch} times less sensitive than such a system.

The reason that a narrowband beam will yield a spectrum with a higher signal-to-noise ratio than a broadband beam is that the noise at a given wavelength in the spectrum is not proportional to the signal level at that wavelength (as in the case of conventional spectrometers). For a FTS, the noise in the spectrum (in the photon-limited case) is a constant whose value is proportional to the square root of the mean flux level in the entire interferogram. Thus, restricting the bandpass and recording a narrowband interferogram serves to filter the noise from the spectrum without losing any signal.

As with any FTS, data acquisition for the multipixel FTS consists of recording the intensity of the

recombined beams as a function of the delay introduced by the delay lines. In our implementation, the delay lines are moved in approximately uniform steps from some minimum to some maximum delay. At each step, the delay lines remain motionless for some period, allowing the CCD to integrate the intensity of the recombined beam. For the multipixel FTS, the recombined beam is dispersed into N_{ch} spectral channels of width Δs . Thus for any single channel, the data consist of the interferogram intensities, I_d , measured at a set of discrete delays, x_i . Our goal is to infer the spectrum, $\tilde{I}(s)$, from the interferogram data. For clarification, x is the optical delay (*i.e.*, if the delay line moves by 1 cm, the optical delay introduced is $x = 2$ cm).

Apart from a constant (which we ignore in this analysis, but which is relevant to the noise statistics discussed above), the interferogram is simply the inverse cosine transform of the spectrum:

$$I_d(x_i) = \int_{s_{\min}}^{s_{\max}} ds \tilde{I}_t(s) \cos(2\pi x_i s), \quad (1)$$

where $\tilde{I}_t(s)$ are the spectral intensities. The subscript t indicates that $\tilde{I}_t(s)$ is the truth spectrum, and is not known *a priori* to the observers, while the subscript d indicates that $I_d(x_i)$ is the data interferogram and is an observable. Therefore, the goal of this project is to infer $\tilde{I}_t(s)$ based on observations of $I_d(\{x_i\})$.

Strictly speaking, we are considering only the real part of the transform. As described in §3, variants of the algorithm are appropriate depending on the *a priori* knowledge of the location of the central fringe (see below). Otherwise, a full Fourier Transform (*i.e.*, including imaginary portion) would be more accurate.

The total optical delay introduced by the interferometer, Δx , is set by the desired spectral resolution, R_{FTS} :

$$\Delta x = \frac{1}{\delta s} = \frac{R_{\text{FTS}}}{s}, \quad (2)$$

where s is the central wavenumber of the bandpass, and δs is the spacing in wavenumber between adjacent spectral intensities.

The algorithm relies on the Nyquist Theorem to set the maximum allowable step size in delay, δx , to avoid aliasing:

$$\delta x = |x_{i+1} - x_i| < \frac{1}{2\Delta s}, \quad (3)$$

where Δs is the bandwidth of the interferogram from a single spectral channel.

For the conventional broadband FTS, $\Delta s \approx s_{\max}$, so the step size in delay length must be smaller than half the minimum wavelength, or typically a few hundred nm. However, for the multipixel FTS, Δs is smaller by a factor of R_g . In practice, the interferogram is sampled at delay intervals smaller than the

maximum permitted interval: the oversampling rate is γ :

$$\delta x = \frac{R_g}{2\gamma s}. \quad (4)$$

The smaller bandwidth allows us to increase the step size in delay at which we sample the interferogram, and thus to integrate longer at each step. Since R_g can easily reach several thousand, the advantage of the smaller bandwidth can be significant indeed.

A specific comparison will make the advantage clear. Suppose we want to resolve absorption lines in the $\lambda\lambda 400 - 900$ nm spectral region of a solar-type star (requiring $R_{\text{FTS}} \approx 50,000$), and to limit the total observation time to under 1000 s to avoid significant Earth-rotation effects in the spectrum. The desired resolution requires us to sample the interferometer response over an optical path of $\approx R\lambda = (50000)(650 \text{ nm}) \approx 3.25 \text{ cm}$ centered on the maximum of the fringe packet. This “central fringe” is located at the delay where the optical path difference between the photons traversing the two delay lines is zero.

For a conventional FTS, the large bandwidth requires us to sample the interferogram at intervals of $\delta x = 0.36 \mu\text{m}$, requiring a total of $\approx 9 \times 10^4$ measurements to span a total optical delay of 3.25 cm. With the 1000 s time constraint, each measurement is allowed 11 ms integration time. A large telescope would be needed to detect a reasonable signal, and high speed, low readout noise detectors would be needed to provide a reasonable duty cycle.

For the multipixel FTS with 1000 pixels, the interferogram in each spectral channel must be sampled at 0.36 mm intervals, resulting in 90 integrations of 11 s each. In addition to the resulting gain in sensitivity (which obviates the need for a huge aperture), the increased integration time also means that high-speed detectors with low read noise are not required.

3. The Algorithm

At this point, we make two significant departures from conventional approaches to spectral reconstruction from FTS data. The first is that we solve the inverse problem by taking advantage of our knowledge about the forward problem. Given a model spectrum, $\tilde{I}_m(\{s_j\})$, we solve the forward problem by obtaining the interferogram, $I_m(\{x_i\})$, that would result from that model spectrum. The inverse problem is then solved by modifying the model spectrum until the model interferogram obtained from the forward problem best matches the observed data, $I_d(\{x_i\})$. This approach is the opposite of the standard strategy of solving the inverse problem by deconvolving the impulse response from $I_d(\{x_i\})$. The advantages of this

procedure are numerous, including an improved ability to correct for the deleterious effects of finite and realistic sampling, a more honest way to treat noise statistics, and a more Bayesian treatment will afford the ability to incorporate prior information (Bretthorst 1988). However, solving the forward problem generally places higher demands on computer processing, resulting in longer runtimes as compared to deconvolution algorithms.

The second deviation from conventional methodology is that we choose a continuous model spectrum rather than a spectrum that is defined only at discrete points. Conventional methods apply Fourier Transforms to discretely sampled data and return discretely sampled transforms. As we show below, conventional Fourier Transforms introduce substantial artifacts in spectra reconstructed from a sparsely sampled interferogram. This situation is analogous to that seen in direct Fourier inversion of sparse aperture data from imaging spatial interferometers, where distinguishing sidelobe structure from real source structure is problematic. As we will see, the method presented here diminishes the sidelobes by one to two orders of magnitude as compared to direct Fourier inversion.

We present two approaches to estimating spectra from sparsely sampled interferograms. In the first method (hereafter, Method # 1), we allow only the spectral intensities to vary and assume that the position of the central fringe is exactly known. The second method (hereafter, Method # 2) also permits variation of the lag corresponding to the central fringe in the interferogram.

3.1. Method # 1: Variation of the Spectral Intensities

Use of this algorithm assumes that the location of the central fringe is known, and that the interferogram has been shifted in delay so as to force the zero optical path difference to occur at the exact maximum of the central fringe. We begin with an initial model at a set of M spectral intensities, $\tilde{I}_m(\{s_j\})$, where $\{s_j\}$ spans a wavenumber range defined by the edges of a single narrowband channel and M is the ratio of the desired resolving power of the FTS to the resolving power of the grating. All spectral intensities outside this range are not free parameters, and are set to zero. The algorithm is robust in the sense that the final result is very insensitive to the quality of the initial guess of the spectral intensities.

We then approximate the spectrum between s_j and s_{j+1} with a linear interpolation between $\tilde{I}_m(s_j)$ and $\tilde{I}_m(s_{j+1})$. This linear-piecewise model of the spectrum $\tilde{I}_m(s)$ results in an interferogram given by:

$$I_m(x_i) = \sum_{j=1}^{M-1} \int_{s_j}^{s_{j+1}} ds \left[\tilde{I}_m(s_j) + (s - s_j)\Delta_j \right] \cos(2\pi x_i s), \quad (5)$$

where:

$$\Delta_j = \left[\frac{\tilde{I}_m(s_{j+1}) - \tilde{I}_m(s_j)}{s_{j+1} - s_j} \right]. \quad (6)$$

The integral can be solved analytically, so Equation (5) becomes:

$$I_m(x_i) = \sum_{j=1}^{M-1} \left[\alpha_{i,j} \tilde{I}_m(s_j) + \Delta_j \beta_{i,j} \right], \quad (7)$$

where

$$\alpha_{i,j} = \left[\frac{\sin(2\pi x_i s_{j+1}) - \sin(2\pi x_i s_j)}{2\pi x_i} \right], \quad (8)$$

$$\beta_{i,j} = \left[\frac{(s_{j+1} - s_j) \sin(2\pi x_i s_{j+1})}{2\pi x_i} \right] + \left[\frac{\cos(2\pi x_i s_{j+1}) - \cos(2\pi x_i s_j)}{(2\pi x_i)^2} \right]. \quad (9)$$

The constants $\alpha_{i,j}$ and $\beta_{i,j}$ are defined by the sampling in the lag and spectral spaces and need not be recalculated for each iteration. The mean-square difference between the model interferogram and the data interferogram is given by:

$$\chi^2 = \frac{1}{n} \sum_{i=1}^n [I_m(x_i) - I_d(x_i)]^2. \quad (10)$$

We now desire the model spectrum which yields a model interferogram that best matches the data interferogram. We can write this condition as a set of equations minimizing χ^2 :

$$\frac{\partial \chi^2}{\partial \tilde{I}_m(s_j)} = \frac{2}{n} \sum_{i=1}^n [I_m(x_i) - I_d(x_i)] \left(\frac{\partial I_m(x_i)}{\partial \tilde{I}_m(s_j)} \right) = 0. \quad (11)$$

To complete the statement of the problem we need to calculate the derivatives, which are analytic:

$$\left(\frac{\partial I_m(x_i)}{\partial \tilde{I}_m(s_j)} \right) = \alpha_{i,1} - \left(\frac{\beta_{i,1}}{s_2 - s_1} \right) \quad \text{for } j = 1, \quad (12)$$

$$\left(\frac{\partial I_m(x_i)}{\partial \tilde{I}_m(s_j)} \right) = \left(\frac{\beta_{i,j-1}}{s_j - s_{j-1}} \right) + \alpha_{i,j} - \left(\frac{\beta_{i,j}}{s_{j+1} - s_j} \right) \quad \text{for } 2 \leq j \leq M-1, \quad (13)$$

$$\left(\frac{\partial I_m(x_i)}{\partial \tilde{I}_m(s_j)} \right) = \left(\frac{\beta_{i,M-1}}{s_M - s_{M-1}} \right) \quad \text{for } j = M. \quad (14)$$

3.2. Method # 2: Variation of the Spectral Intensities and Central Lag

The interferogram is symmetric about the zero optical path difference since the spectrum itself is real. As a result, one would think that determining the zero optical path difference would be trivial. However, localizing the central lag is significantly complicated by sparse sampling, and the inferred position is generally dependent on the noise level, sampling of the interferogram, and finally, the detailed shape of the

spectrum. In this paper, we assume that the spectrum is unknown, *a priori*. Additional information can be incorporated to improve the convergence of the algorithm, depending on the application.

In Method # 2, we allow the central lag as well as the spectrum to vary. As expected, this process provides more information than Method # 1, at the cost of reduced numerical stability: as we will see, a noiselike initial guess for the spectrum and, more importantly, a random guess for the central lag, are not always sufficient to properly reconstruct the spectrum and central lag.

We proceed exactly as above, except that we explicitly write an expression for χ^2 as a function of ϵ , the lag corresponding to the zero optical path difference in the interferogram [*i.e.*, $I = I(x - \epsilon)$]:

$$\chi^2 = \frac{1}{n} \sum_{i=1}^n [I_m(x_i - \epsilon) - I_d(x_i)]^2. \quad (15)$$

The derivatives of χ^2 with respect to $\tilde{I}(s)$ are the same as in Method # 1, except that $I_m = I_m(x_i - \epsilon)$.

The additional derivative that is relevant to the solution of this problem is given by:

$$\frac{\partial (\chi^2)}{\partial \epsilon} = \frac{2}{n} \sum_{i=1}^n [I_m(x_i - \epsilon) - I_d(x_i)] \left(\frac{\partial I_m(x_i - \epsilon)}{\partial \epsilon} \right) = 0, \quad (16)$$

where:

$$\frac{\partial I_m(x_i - \epsilon)}{\partial \epsilon} = \frac{1}{x_i - \epsilon} \sum_{j=1}^{M-1} \left(A_{i,j} \tilde{I}_m(s_j) + B_{i,j} \Delta_j \right), \quad (17)$$

and:

$$A_{i,j} = -s_{j+1} \cos(z_i s_{j+1}) + s_j \cos(z_i s_j) + \frac{\sin(z_i s_{j+1})}{z_i} - \frac{\sin(z_i s_j)}{z_i}, \quad (18)$$

$$\begin{aligned} B_{i,j} = & s_j s_{j+1} \cos(z_i s_{j+1}) + (2s_{j+1} - s_j) \frac{\sin(z_i s_{j+1})}{z_i} - s_j \frac{\sin(z_i s_j)}{z_i} \\ & - s_{j+1}^2 \cos(z_i s_{j+1}) + \frac{2 \cos(z_i s_{j+1})}{z_i^2} - \frac{2 \cos(z_i s_j)}{z_i^2}, \end{aligned} \quad (19)$$

and we have used the definition $z_i = 2\pi(x_i - \epsilon)$. In this implementation, $A_{i,j}$ and $B_{i,j}$ (analogous to $\alpha_{i,j}$ and $\beta_{i,j}$ in Method # 1) are functions of the sampling in the lag and spectral domains, as well as ϵ .

3.3. Algorithm Evaluation

Below, we test the performance of method presented in this paper by comparing the inferred spectra to the truth spectrum. We can now use any of a number of minimization techniques to solve Equations (11)—(14) and/or Equations (16)—(19), especially since the derivatives are analytic. Our implementation uses a simple Newton method. If the result of the algorithm is strongly affected by the initial guess (*i.e.*,

there are many local extrema), then a more complex searching method must be used to locate the global solution. Fortunately, resorting to grid searches is often not necessary given the quality of the *a priori* information available.

To test our implementation of the algorithms, we begin with a truth spectrum, $\tilde{I}_t(s)$, given by a unit amplitude square wave between 1.666 and 2.0 μm^{-1} (corresponding to 0.6 to 0.5 μm wavelength) plus two Gaussian absorption lines with depths 0.3 and 0.6, widths of 0.02 μm^{-1} each, and centered at 1.85 μm^{-1} and 1.75 μm^{-1} , respectively (see Figure 4, solid line). Using Equation (4), we generate the data interferogram, $I_d(\{x_i\})$, which we sparsely sample at 1.2 μm intervals (Figure 2). The central fringe contains between five and six oscillations, although none have been resolved due to the sparse sampling.

We begin the optimization by selecting an initial spectrum which is white Gaussian noise, as shown in Figure 3. Using Method # 1, we infer the best spectrum (in a least squares sense) in 15 seconds using a 500 MHz Pentium computer running IDL. In the case of Method # 2, we use the initial spectral guess in Figure 3 as well as an estimate of the central lag position that is in error by 20 nm. The optimization using Method # 2 requires a significantly longer runtime (5.3 minutes), and results in a spectrum that is superior (in a χ^2 sense), but still very similar to that inferred by Method # 1. These two spectra are plotted as a single dotted line in Figure 4 since they are indistinguishable on the scale of the plot. For comparison, the results from a traditional, direct cosine transform were generated and are shown for comparison as the dashed line in Figure 4.

We then compare the reconstructed spectrum to the truth spectrum to assess the performance of the algorithm. We show the truth minus reconstructed residuals in Figure 5. Again, the results from Method # 1 and # 2 are indistinguishable on the scale of the plot and are shown as a single dotted line. For comparison, the residuals from the Fourier inversion are shown as a dashed line. As a final diagnostic, we plot the absolute value of the ratio of the Method # 1 (2) residuals to the Fourier inversion residuals as dotted (solid) lines in Figure 6. The example shown here is typical of the tests that have been processed so far.

4. Discussion

There are two new aspects of our approach to spectral inference. The first is multiplexing a Fourier Transform Spectrometer by dividing the white light beam into numerous narrowband beams. The second is choosing to infer the spectrum from each channel using the algorithm presented in this paper. We

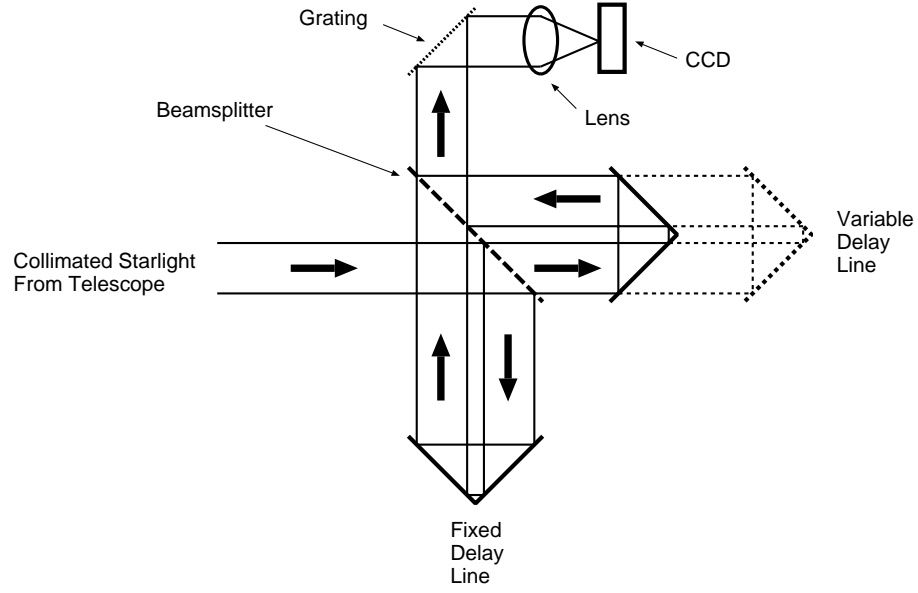


Fig. 1.— A schematic representation of the light path for a multiplexed FTS. Only one output of the beamsplitter is shown.

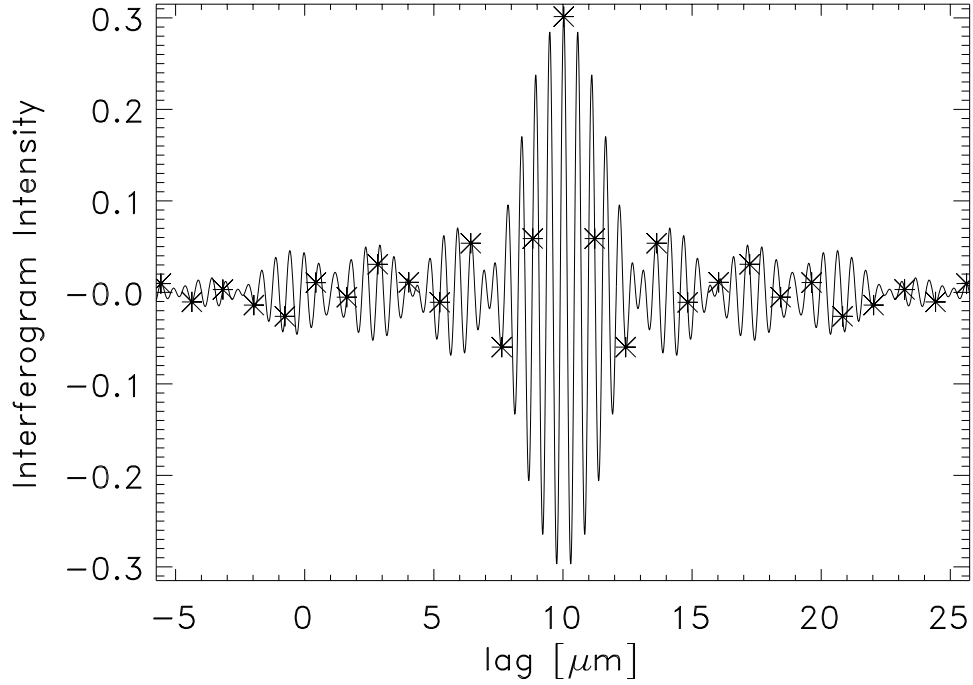


Fig. 2.— A portion of the sparsely sampled interferogram. The mean level has been subtracted. The underlying function is shown as a solid line, and the data which span -50 to -70 μm are represented by the asterisks. The central fringe packet is unresolved in the sampled interferogram.

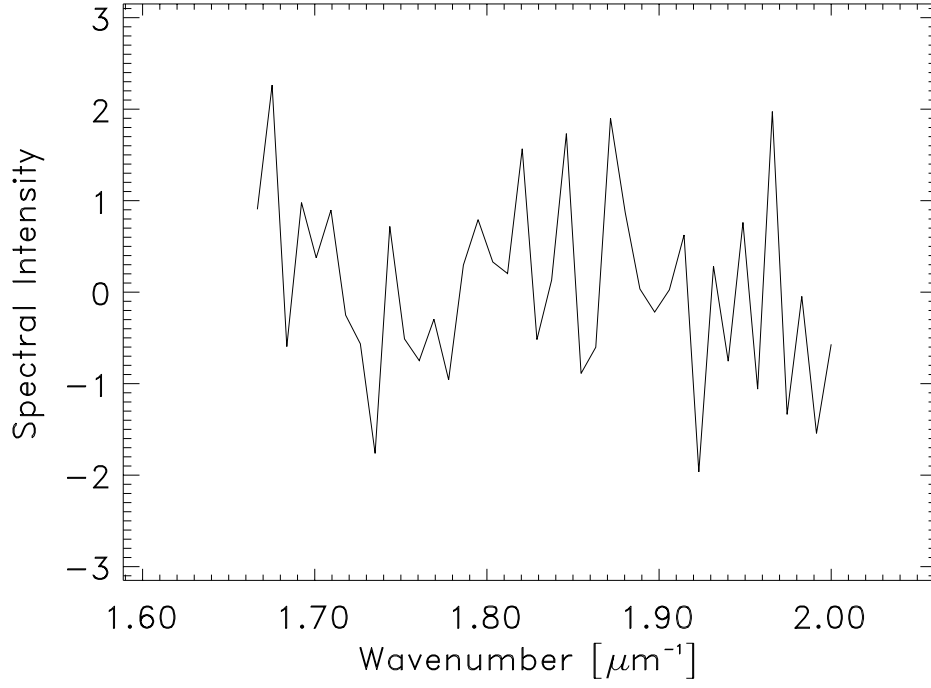


Fig. 3.— The initial guess at the spectrum. This guess is Gaussian random noise. All derived spectral information therefore comes from the interferogram and is not biased by the initial guess.

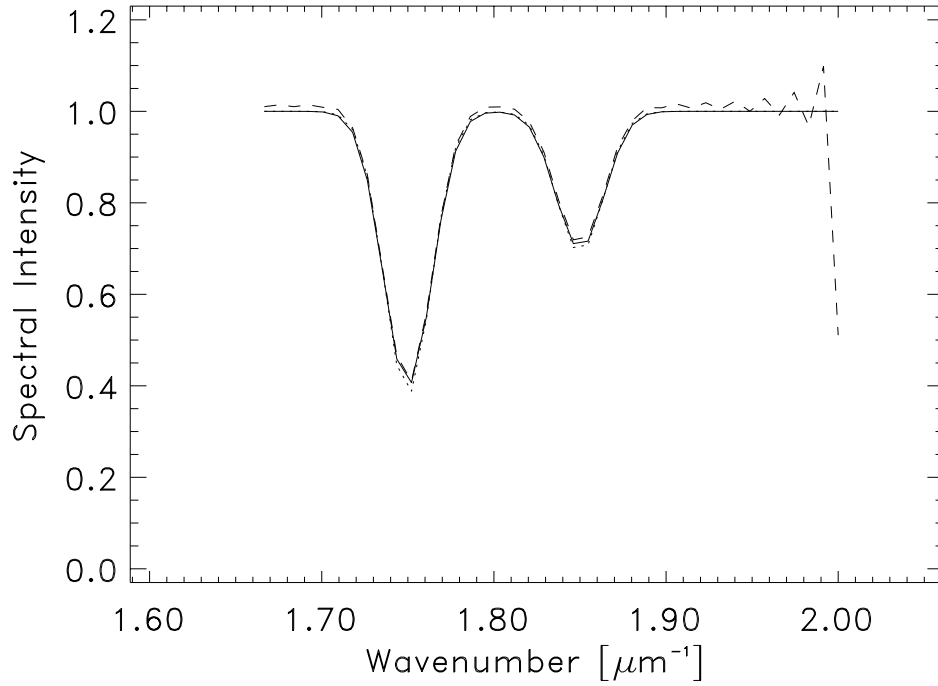


Fig. 4.— The truth spectrum (solid line: see §3.3 for details), inferred spectra from Method # 1 and # 2 (the curves are indistinguishable on this scale and are shown as a single dotted line) and from DFT inversion (dashed line). The sparse sampling reconstructions are difficult to distinguish from the truth spectrum.

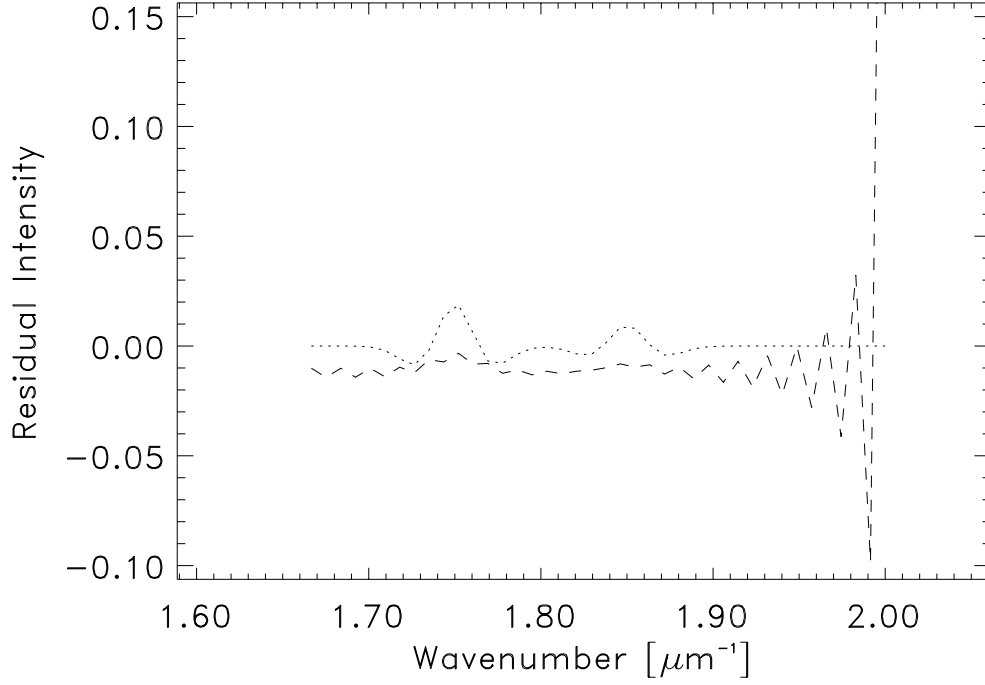


Fig. 5.— The residuals (truth minus reconstruction) from Method # 1 and Method # 2 are indistinguishable in this plot (dotted line), and are smaller than the residuals resulting from Fourier inversion (dashed line).

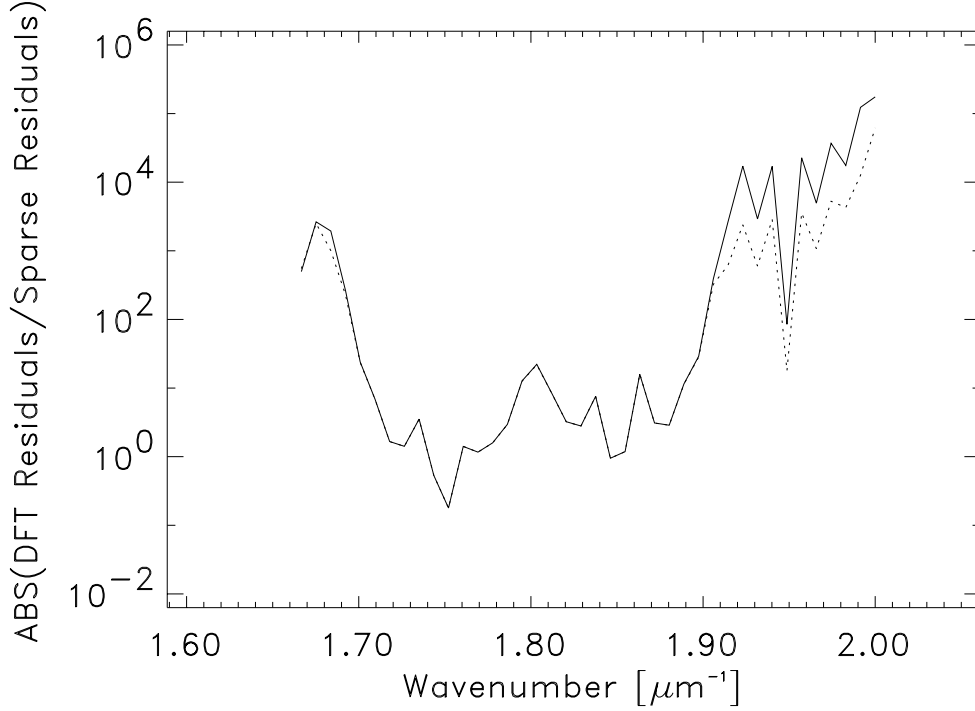


Fig. 6.— The ratio of the residuals from the DFT inversion to the residuals from Method # 1 (dotted line) and Method # 2 (solid line). The magnitude of the residuals is many times larger for the DFT inversion than for the algorithms presented in this paper across most of the spectrum.

separately treat the distinguishing characteristics and implications of both choices below.

4.1. Multiplexing a FTS

Multiplexing the spectrometer by dispersing the white light beam requires that some components be added to the optics train; these hardware modifications are not within the scope of this paper and will be fully described in a future publication. However, the added instrumental complexity is fully compensated by multiple important benefits. The narrow bandwidth of each channel allows for much sparser sampling of the interferogram (by a factor of N_{ch}), resulting in longer integration times per delay setting. This eliminates considerations of the detector read noise, which would otherwise be a critical factor limiting the achievable signal-to-noise ratio. An additional systemic improvement is bestowed on the duty cycle for a multiplexed FTS. One of the chief contributors to experimental overhead is the dead time incurred while waiting for vibrations in the delay line to damp at the termination of a slew. The smaller number of interferogram samples for a multiplexed FTS translates to diminished overhead and improved duty cycle. In terms of data products, the narrow bandpasses of a multiplexed FTS can be used to better correct for chromatic phenomena, including differential dispersion (due, *e.g.*, to optical path differences in air), as compared to a conventional FTS.

Finally, the most significant improvement from multiplexing a FTS is that the signal-to-noise ratio of the spectrum improves by a factor of $\sqrt{R_g}$ as compared to a conventional FTS (Brault 1985; Maillard 1988). This can be shown as follows. Consider a telescope collecting a stellar flux of W photons $\text{s}^{-1} \text{nm}^{-1}$ (we have expressed W using units of wavenumber instead of wavelength). An interferogram with measurements at N_{lag} delays is obtained with a mean level of $W t_{\text{lag}} \Delta s$ photons per lag for a given spectral channel, where $\Delta s = s/R_g$ is the bandwidth of the channel, and t_{lag} is the integration time at each delay. The spectral resolving power implied by the maximum optical path difference is given by equation (2). In the following analysis, we consider the data from a single spectral channel. Since the integral of the spectral intensities over the total spectral bandwidth is equal to the intensity, I_o , at the peak of the central fringe of the interferogram the mean spectral intensity (*i.e.*, the mean signal level of the spectrum) is just I_o divided by the spectral bandwidth. Assuming that the fringe contrast is 100%, then I_o is just equal to the mean level of the interferogram, and the mean spectral intensity is:

$$S_S = W t_{\text{lag}}, \quad (20)$$

On average, the noise level in the interferogram is determined according to Poisson statistics:

$$\sigma_I = \sqrt{W t_{\text{lag}} \Delta s}. \quad (21)$$

Parseval's Theorem states that the total noise power in the spectral and lag domains is equal:

$$\sigma_S = \sigma_I \sqrt{\frac{\Delta x}{\Delta s}} \quad (22)$$

where σ_S is the average spectral noise power per pixel, and σ_I is the average noise power in the interferogram per pixel. We combine Equations (2), (20), (21) and (22) to compute the signal-to-noise ratio in the spectrum:

$$SNR_S = \sqrt{\frac{W t_{\text{lag}} s}{R_{\text{FTS}}}}. \quad (23)$$

Not surprisingly, the number of samples in the interferogram (N_{lag}), is directly proportional to the number of independent spectral values, M , across one channel:

$$M = \frac{R_{\text{FTS}}}{R_g} = \frac{2N_{\text{lag}}}{\gamma}, \quad (24)$$

and Equation (23) becomes:

$$SNR_S = \sqrt{\frac{2W t_{\text{lag}} N_{\text{lag}} s}{\gamma R_{\text{FTS}} M}}. \quad (25)$$

For the case of the conventional FTS, $R_g = 1$.

Since the width of the central fringe packet is inversely proportional to M , small values of M mean that meaningful signal is collected throughout a larger portion of the interferogram. A large value of M suggests a narrow fringe will be the only region in the interferogram that has significant signal. In effect, M serves to dilute the signal as the fringes decorrelate. Equation (25) demonstrates that SNR_S is directly proportional to $\sqrt{R_g}$ for a constant integration time ($t_{\text{lag}} N_{\text{lag}}$), source brightness (W), observing wavenumber (s), and spectral resolving power (R_{FTS}). Sensitivity is gained with greater multiplexing.

As mentioned in §2, a conventional FTS requires much longer integration times to achieve the same signal-to-noise ratio as a multiplexed device with the same characteristics. To emphasize this point, we use the equations derived above to consider a 1 m telescope with perfect throughput observing a $m_V = 5$ star.

In the case of the conventional FTS ($R_g = 1$) with a bandpass of 500 nm, every interferogram consists of 90,000 integrations each lasting 11 ms. A mean level of 3.9×10^6 photons would be detected per lag, resulting in a signal-to-noise ratio in the interferogram of approximately 2000. With $M = 50,000$ and $N_{\text{lag}} = 90,000$, the signal-to-noise ratio of the resulting spectrum is 12.

For the case of a multiplexed FTS with 1000 channels ($M = 50$) and a bandpass of 500 nm, each interferogram consists of just 90 integrations with each integration lasting 11 s. Again, a mean level of 3.9×10^6 is detected per lag, resulting in a signal-to-noise ratio in the interferogram of approximately 2000. However, the signal-to-noise ratio of the resulting spectrum is 370 (this assumes $\gamma = 1$). The increase in the signal-to-noise ratio of the spectrum is proportional to $\sqrt{R_g}$, and is due to the noise filtration arising from the bandwidth-limited nature of the interferogram. This situation is the exact opposite of what is encountered with conventional dispersing spectrometers, in which case detecting dispersed light dilutes the signal-to-noise ratio (per pixel) as compared to detecting the white light beam.

The above example even more strongly favors our algorithm when the overheads due to vibration mitigation after a slew, readout, etc. are considered.

4.2. The Algorithm

One of the chief advantages of the algorithm presented in this paper is that it advantageously utilizes additional information to better constrain inferred parameters. For example, we know that the interferogram for each channel is bandwidth-limited. As a result, the algorithm permits the spectral intensities to vary *only* between the band edges. Outside, the spectrum is set identically to zero. As such, the algorithm functions between the two classical limits of “model fitting” and “pure imaging”. The less knowledge about the band edges, the more parameters that are required to be fit. Also, the algorithm has similarities to other, more commonly used mapping algorithms. Inferring the spectrum between two wavenumber boundaries is similar to identifying CLEAN components within a CLEAN box. The algorithm naturally imposes locality (*i.e.*, the spectral energy distribution is bandwidth-limited) in the spectrum: this assumption is critical, since the solution of spectra from sparse interferograms (or images from sparse spatial interferometer data) is not mathematically unique otherwise.

The algorithm also models the spectrum as a piecewise continuous function instead of a set of narrow delta functions available to Fourier techniques. The model thus more accurately describes reality, and should in principle result in more accurate spectral inferences. In addition, since residuals between the model and the data also contain information regarding the noise, solving the forward problem allows a more honest treatment of the noise statistics.

For the sampling rates quoted in this paper, the χ^2 surface is smooth enough for both methods (§§3.1, 3.2) to localize the global maximum in virtually all cases. The only exception happens when the initial

guess for the central lag is very far ($> \lambda/4$) from the true value. However, we can determine the central lag *a priori* by using a white light calibration source, and we can use Method # 2 to infer the central fringe position. By contrast, FFT algorithms can result in significant errors if the central fringe position is not precisely known. With Method # 2, we expect to be able to localize the lag corresponding to the central fringe with a precision of:

$$x_{\text{cf}} \approx \frac{\lambda}{4SNR_1} \approx \frac{150 \text{ nm}}{SNR_1}. \quad (26)$$

Typical values of $SNR = 100$ suggest that $x_{\text{cf}} \approx 2 \text{ nm}$, while our tests have utilized 20 nm to be conservative (see §3.2). This precision is valid for a single, narrowband spectral channel. A more precise position for the central fringe can be obtained by averaging the central fringe positions for all 1000 spectral channels (after correcting for the effects of differential dispersion due to optical path mismatches in air).

5. Summary and Conclusions

We have demonstrated two variants of an algorithm for inferring a spectrum whose interferogram best matches observed data from a dispersed FTS. The algorithm uses *a priori* knowledge that the interferogram is spectrally bounded to reconstruct the spectrum. The narrowband nature of the interfering light enables us to sample the interferogram sparsely, as allowed by the Nyquist Theorem for band limited signals. The broadband spectrum consists of the sum of the inferred narrowband spectra. The algorithm is robust, yielding a final spectrum that is insensitive to the initial spectral guess, and whose impulse response has smaller sidelobes than conventional Fourier inversion methods.

The practical consequences for multiplexed FTS devices are significant, especially in obviating the need for a fast-readout, low read-noise array detectors. The requirement of millisecond-timescale integrations relaxes to second-timescale integrations, and the required number of integrations is reduced by the same factor. In addition, since a large fraction of the observing overhead (*e.g.*, CCD readout, waiting for vibrations to damp before starting an integration, etc.) is directly proportional to the number of integrations in an interferogram and the fractional overhead is inversely proportional to the integration time, sparse sampling improves the instrumental duty cycle by a large factor.

Future modifications of the algorithm are easy to envision. For example, increasing the order of the spectral interpolation to quadratic or cubic functions is likely to yield small improvements in the quality of the fit to the interferogram. In addition, more complex versions of multiplexed FTS instrumentation, perhaps including imaging capabilities, could benefit from a variant of the algorithm to accurately

reconstruct spectral images of astrophysical targets.

6. Acknowledgements

We would like to thank several individuals who have made invaluable contributions to the multipixel FTS project, for without their help, this paper would not have been published. This group includes B. Behr, J. Benson, J. Bowles, B. Burress, T. Corbin, J. Clark, C. Denison, C. Ekstrom, F. Gauss, L. Ha, S. Horner, D. Hutter, K. Johnston, G. Kaplan, T. Klayton, R. McMillan, R. Millis, S. Movit, T. Nordgren, T. Pauls, S. Petrossian, J. Pohlman, T. Rafferty, C. Sachs, T. Siemers, D. Smith, J. Sudol, L. Rickard, S. Urban, G. Wieder, N. White, and L. Winter. Partial support for this research was provided by a grant from NASA in conjunction with the SIM Preparatory Science Program (NRA 98-OSS-07), and by the IDU/IS/CICT Program, NASA Aerospace Technology Enterprise.

References

- Baranne, A., Queloz, D., Mayor, M., Adrianzyk, G., Knispel, G., Kohler, D., Lacroix, D., Meunier, J.-P., Rimbaud, G., & Vin, A. 1996, *A&AS*, 119, 373.
- Bretthorst, G.L. 1988, in *Bayesian Spectrum Analysis and Parameter Estimation*, Springer-Verlag, p.3.
- Brault, J.W. 1985, in *High Resolution in Astronomy*, 15th Advanced Course of the Swiss Society of Astrophysics and Astronomy, eds. A. Benz, M. Huber and M. Mayor, (Geneva Observatory: Sauverny), p. 3.
- Butler, R.P., Marcy, G.W., Williams, E., McCarthy, C., Dosanji, P., & Vogt, S.S. 1996, *PASP*, 108, 500.
- Cumming, A., Marcy, G.W., & Butler, R.P. 1999, *ApJ*, 526, 890.
- Erskine, D., Edelstein, J., Feuerstein, W.M., & Welch, B. 2003, *ApJ Lett.*, 592, 103L.
- Maillard, J.-P. 1988, in *The Impact of Very High S/N Spectroscopy on Stellar Physics*, eds. G. Cayrel de Strobel and M. Spite, p. 71.
- Marcy, G.W., & Butler, R.P. 1998, *ARA&A*, 36, 57.